

Review Paper

Structure-Zone Modeling of Sputter-Deposited Thin Films: A Brief Review

Received November 15, 2019; accepted November 27, 2019

Eiji Kusano*

Advanced Materials Center, Kanazawa Institute of Technology, Ishikawa 9240838, Japan

*Corresponding author E-mail: kusano@neptune.kanazawa-it.ac.jp

ABSTRACT

In this paper, the structure zone model (SZM) for sputter-deposited thin films is reviewed through a systematic discussion of the dependence of film structure and properties on the discharge pressure and homologous substrate temperature. The SZM is applicable to the sputter-deposited metal and metal oxide thin films with a film thickness ranging from a few to several hundred nanometers. Furthermore, the SZM is evolved for the sputter-deposition of films through energization of the sputtered particles by replacing the axis of the deposition pressure with that of the effective energy per depositing atom. The results suggest that the SZM is valid as a conceptual diagram with respect to optimizing film-deposition conditions for industrial applications.

Keywords: Structure zone model, Sputtering

I. Introduction

Thin films deposited by sputtering generally possess an open-voided columnar structure depending on the deposition conditions such as substrate temperature and discharge pressure [1–3]. The open-voided structures determine the film properties, such as electrical resistivity, film stress, and refractive index. Accordingly, it is necessary to understand the dependence of the resultant film structure and its properties on the film deposition conditions for optimizing the film properties that can satisfy the device-fabrication requirements for industrial applications. From this viewpoint, the structure zone model (SZM) was proposed by Thornton [4–6] by considering the dependence of the film structure and properties on the discharge pressure and homologous substrate-temperature that is based on the structure model for vacuum-evaporation-deposited thin films [7]. The SZM was established by superimposing the film texture on the internal structure of thick metal films (thickness $>1\ \mu\text{m}$), where the film texture represents the film structures formed as a result of the aggregation of atoms or clusters on the substrate surface, mainly in the range of a few tens to hundreds of nanometers. The internal structure in the model is the crystallographic structure formed within the aggregated film-texture.

Since the initial proposal of the SZM by Thornton, the structure and properties of thin films have been widely discussed on the basis of this model [8–12]; however, a systematic evaluation describing the changes in film structure and properties as a function of homologous substrate-temperature irrespective of the thin-film materials is yet to be conducted. In this context, Kusano reported that the structure and properties of group-IV thin-metal films [13] and oxide films [14] could both be categorized as functions of homologous substrate-temperature using the SZM, which is applicable to thin metal and oxide films with approximately several hundred of nanometers thick-

nesses.

In this review, the applicability of the SZM for the metal and oxide thin films is demonstrated in terms of the dependence of film structure and properties on the discharge pressure and homologous substrate-temperature.

II. Structure Zone Model

The SZM exhibits film structure and properties as functions of discharge pressure and homologous substrate-temperature, represented by T_{sub}/T_m , where T_{sub} denotes the substrate temperature and T_m denotes the melting point of the deposited thin-film material. The resultant values are categorized into four zones as shown in Fig. 1:

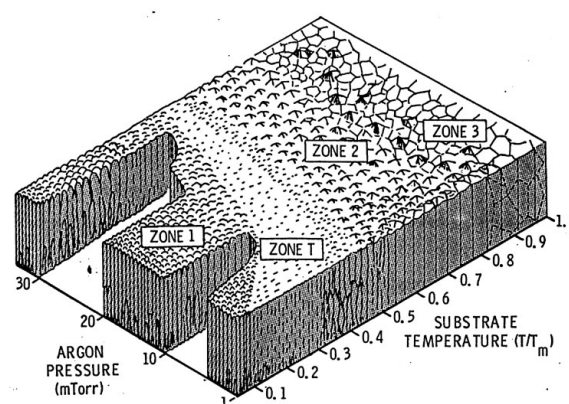


Figure 1. Structure zone model representing the effects of homologous substrate temperature and Ar discharge-gas pressure on the structure of metal films deposited by magnetron sputtering (Thornton [6], Copyright 1974, American Vacuum Society).



Zone 1, Zone T, Zone 2, and Zone 3 [4–6].

In Zone 1, the thin-film texture is an open-voided tapered fibrous structure, which is resulted from the low-angle oblique incidence of the thermalized particles and the limited diffusion of adatoms on the substrate surface. The former is the result of the collision between the sputtered particles and discharge-gas particles during the transportation of the sputtered particles from the target surface to the substrate, which is constitutional in the sputter-deposition, and the latter is the result of the low substrate temperature. As a result of the limited surface diffusion of adatoms, the crystallographic structure is amorphous. The area of Zone 1 versus T_{sub}/T_m (Fig. 1) is wider at high discharge pressures because the scattering of the sputtered particles due to discharge-gas particles is highly likely at high discharge pressures. The Zone 1 can be observed at $T_{\text{sub}}/T_m < 0.1$ or 0.2 at discharge pressures < 0.5 Pa and at $T_{\text{sub}}/T_m < 0.4$ at the discharge pressure of 4 Pa.

In Zone T, the film texture changes into wider columns with flat surfaces. This is due to the further promotion of the thermally enhanced surface diffusion owing to an increase in the substrate temperature by the energetic particle bombardment. In other words, the Zone T structure forms due to the manifestation of the interaction between the thermally enhanced surface diffusion and the bombardment of the energetic particles. The promoted diffusion fills the space between columns and the bombardment makes the column surface flat. However, the surface and bulk diffusions are still limited because of the relatively low substrate-temperature, resulting in the amorphous crystallographic structure in the columns. For the vacuum-evaporation-deposited thin films, the Zone 1 is expected to be observed as predicted by the SZM. The Zone T can be observed at 0.1 or $0.2 < T_{\text{sub}}/T_m < 0.3 - 0.35$ for discharge pressures < 0.5 Pa and at $0.4 < T_{\text{sub}}/T_m < 0.5 - 0.55$ for the discharge pressure of 4 Pa.

In Zone 2, the thermal surface and grain-boundary adatom diffusions increase with an increase in substrate temperature, which, in turn, widens the columns and reduces the spaces between the columns further. The enhanced surface diffusion, compared with the reconstruction by energetic-particle bombardment, significantly promotes crystallographic growth in the columns, resulting in a higher crystallinity. The columns grow with a preferred orientation based on the deposition conditions and materials. In Zone 2, the film properties are comparable with those of the bulk material mainly because of the thin spaces between the columns. The high rates of thermal surface and grain-boundary diffusions reduce the effect of discharge pressure on the film texture. The Zone 2 can be observed at $0.3 - 0.35 < T_{\text{sub}}/T_m < 0.7$ for discharge pressures < 0.5 Pa and at $0.5 - 0.55 < T_{\text{sub}}/T_m < 0.7$ for the discharge pressure of 4 Pa.

In Zone 3, the enhanced bulk and boundary adatom diffusions dominate the formation of the film texture and internal structure. As a result, the spaces between the column boundaries narrow and the internal thermal crystallization of the columns occurs, resulting in near-equiaxed and highly crystallized internal-structures, especially at high T_{sub}/T_m . In Zone 3, the discharge pressure has negligible effect on the film texture formation. Therefore, the boundary between Zone 2 and Zone 3 is essentially independent of the discharge pressure. The Zone 3 can be observed at $0.7 < T_{\text{sub}}/T_m$ for the entire discharge-gas pressure range.

The existence of Zone T between Zone 1 and Zone 2 is a special feature associated with the SZM for the sputter-deposited thin films and not the vacuum-evaporation-deposited thin films. In Thornton's

first two papers [4,5], the effect of energetic-particle bombardment on the structure of Zone T was not well addressed. In the later reports [15,16], he discussed the energy transferred to the substrate by the energetic-particle bombardment in the sputter-deposition, which was also addressed in his study on the sputter-deposited films [6]. Generally speaking, except for Messier *et al.* [9], the effects of energetic-particle bombardment on film structure and properties have not been discussed in the existing literature [8,10,11].

For industrial applications, a low substrate temperature is favorable in order to reduce the processing costs as well as to meet the substrate's heat-tolerance limitations; however, when the substrate temperature is increased, the deposition process approaches thermal equilibrium, resulting in favorable film properties, such as low stress, high refractive index, and low resistivity. For obtaining a high density of the thin films deposited onto a substrate at low temperatures, the discharge pressure should be lower than 1 Pa, as suggested by the SZM. In other words, thin films are deposited under Zone T conditions at low ranges of T_{sub}/T_m in industrial applications. Therefore, it is extremely important to understand the mechanism of thin-film deposition in Zone T for most industrial applications.

III. Structure and Properties of Sputter-Deposited Metal and Oxide Thin Films

In this section, the effects of discharge pressure and homologous substrate-temperature on the film structure and properties will be reviewed by referring to the previously reported data [13,14,17,18]. Accordingly, the appropriateness and applicability of the SZM is demonstrated for metal and oxide thin films deposited by sputtering.

1) Effects of Discharge-pressure

At low homologous substrate temperatures, the dominant factor affecting film structure is the discharge pressure. Figure 2 shows the cross-sectional scanning electron microscopy (SEM) images of the Ti thin films deposited by magnetron sputtering at discharge pressures of 0.5, 1.0, 1.5, and 2.0 Pa without heating the substrate, i.e., at T_{sub}/T_m of approximately 0.15 [17]. The cross-sectional SEM images describe the

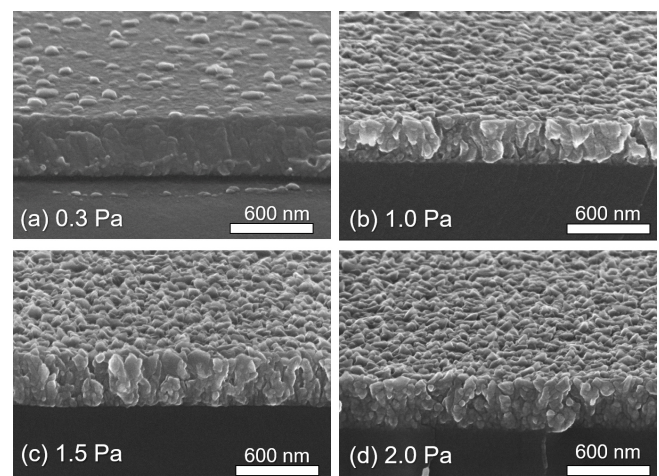


Figure 2. Cross-sectional SEM images of Ti thin films deposited by magnetron sputtering at discharge pressures of 0.5, 1.0, 1.5, and 2.0 Pa without heating the substrate. T_{sub}/T_m is approximately 0.15 (Oya and Kusano [17]).

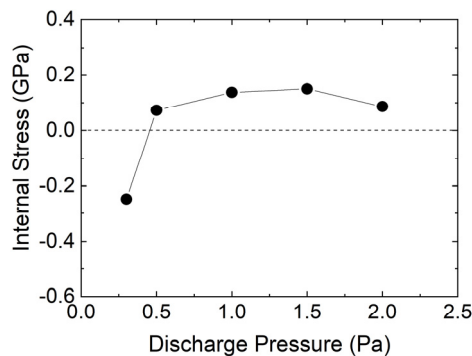


Figure 3. Internal stress of Ti thin films as a function of discharge pressure. The internal stress was calculated using the lattice strain evaluated by X-ray diffraction (XRD) measurements. The solid line between data points is an eye guide (Data from Oya and Kusano [17]).

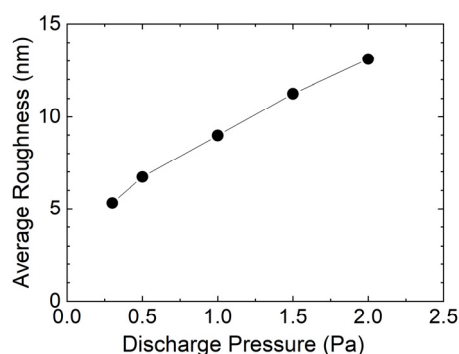


Figure 4. Surface-roughness of Ti thin films as a function of discharge pressure. The solid line between data points is an eye guide (Data from Oya and Kusano [17]).

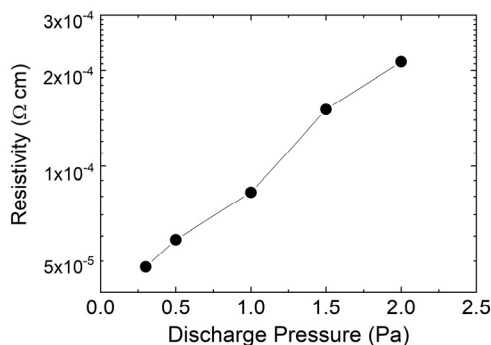


Figure 5. Resistivity of Ti thin films as a function of discharge pressure. The solid line between data points is an eye guide (Data from Oya and Kusano [17]).

change from a Zone T structure to a Zone 1 structure. Obviously, as a result of the change in film texture, the film properties also change. Figure 3 shows the internal stress of the Ti thin films as a function of discharge pressure [17], from which it is evident that the internal stress transitioned from compressive to tensile between discharge pressures of 0.3 and 0.5 Pa. Figure 4 shows the surface-roughness of the Ti thin films as a function of discharge pressure [17]. It is evident from Fig. 4 that the surface roughness increases with an increase in the discharge pressure. Figure 5 shows the resistivities of the Ti thin films as a function of discharge pressure [17]. The resistivity of the

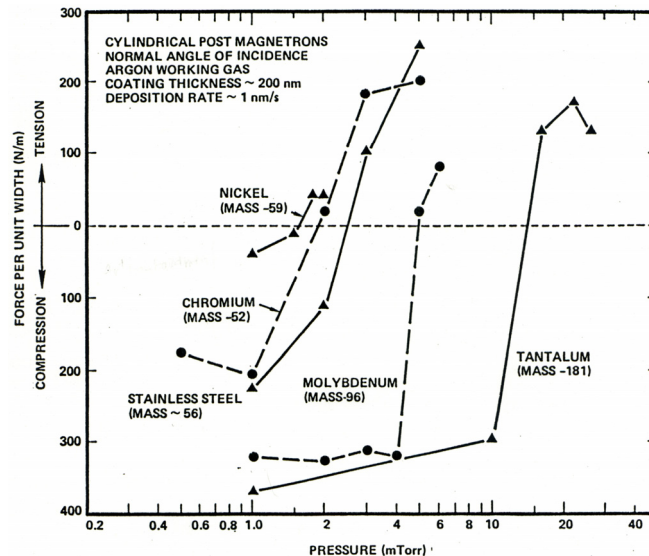


Figure 6. Force per unit width of Ni, Cr, stainless steel, Mo, and Ta thin films as a function of discharge pressure (Thornton and Hoffman [19], Copyright Elsevier B.V.).

bulk Ti is $3.9 \times 10^{-5} \Omega \text{ cm}$. As a result of the open-void formation in the film texture, the resistivity increases with an increase in the discharge pressure. The results shown in Figs. 4 and 5 indicate no abrupt transitions between Zone T and Zone 1, whereas an abrupt transition is observed from Zone T to Zone 1 in Fig. 3 at a discharge pressure of approximately 0.5 Pa.

The film-stress transition points depend on the film material mass or the ratio of the film material mass to the discharge gas mass in addition to the discharge pressure. However, the dependence of the transition points on the film material mass is not discussed in the SZM. Figure 6 shows the force per unit length of approximately 200-nm thick Ni, Cr, stainless steel, Mo, and Ta thin films as a function of discharge pressure [19], which displays the effect of particle mass on the stress-pressure curve. For all the materials, with an increase in the discharge pressure, Zone T stress (compressive) changes to Zone 1 stress (tensile). Concerning the film mass, with an increase in the particle mass, the pressure at which the compressive-stress-tensile-stress transition occurs shifts to a higher discharge pressure; however, the shape of the stress-discharge curve remains nearly the same, irrespective of the film material. The reason for the shift is that the ratio of higher film mass to high discharge gas mass reduces the loss of the particle energy. The shift in the transition point demonstrates that the Zone 1 - Zone T boundary shifts with the change in the film mass or the ratio of the film mass to discharge gas mass.

The discharge pressure also affects the film structure and properties in the oxide deposition. The reactive-sputter-deposited TiO_2 thin films show an increase in the surface roughness with increasing discharge pressure, as shown in Fig. 7 [18]. Moreover, the internal stress of the TiO_2 thin films changes from compressive to tensile, as displayed in Fig. 8 [18]. This tendency is in accordance with the metal thin films. The refractive index, as shown in Fig. 9, decreases with an increase in the discharge pressure due to the promotion of the open-voided structure [18]. The same results can be inferred from the SEM observations, where the cross-section of the TiO_2 thin film exhibited an open-voided columnar structure at discharge pressures of 1.5 and 3.0 Pa and a fine columnar structure at a discharge pressure

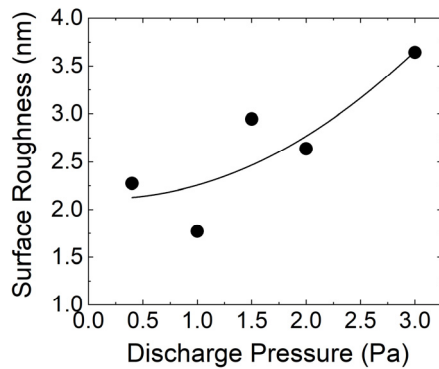


Figure 7. Surface roughness of TiO_2 thin films deposited by reactive sputtering as a function of discharge pressure. The solid line between data points is an eye guide (Sakamoto *et al.* [18]).

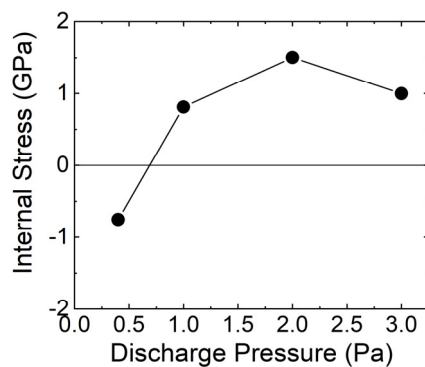


Figure 8. Internal stress of TiO_2 thin films deposited by reactive sputtering as a function of discharge pressure. The solid line between data points is an eye guide (Sakamoto *et al.* [18]).

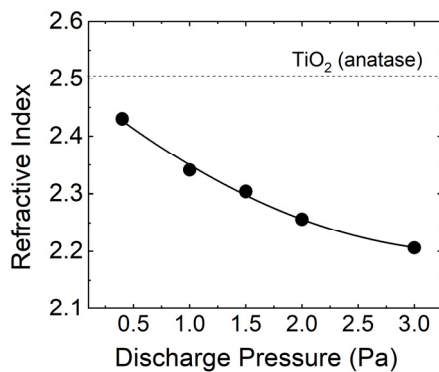


Figure 9. Refractive index of TiO_2 thin films deposited by reactive sputtering as a function of discharge pressure. The solid line is an eye guide (Sakamoto *et al.* [18]).

of 0.4 Pa [18]. The open-voided structure results in the instability of the refractive index when exposed to water vapor. Therefore, in industrial applications, the disadvantages of open-voided structures of films deposited at high discharge pressures should be considered.

2) Effects of homologous substrate temperature

The substrate temperature is the most influential factor in thin film deposition. Changes in the structure, particularly the columnar

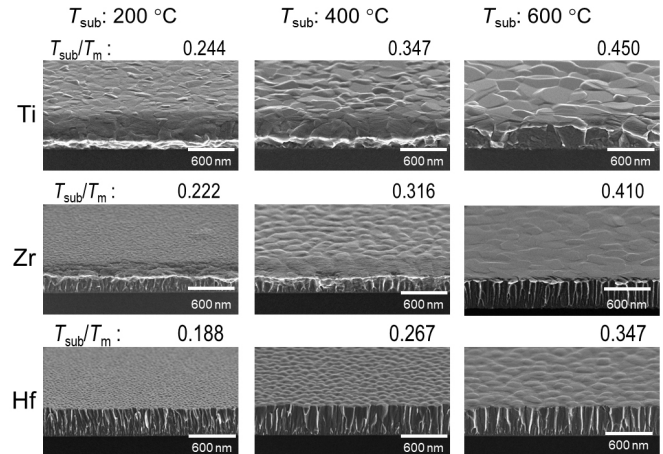


Figure 10. Cross-sectional SEM images of Ti, Zr, and Hf thin films deposited at substrate temperatures of 200, 400, and 600 °C (Kusano [13]).

structure, are primarily demonstrated by cross-sectional SEM images. Figure 10 shows the cross-sectional SEM images of the Ti, Zr, and Hf thin films deposited at $T_{\text{sub}} = 200, 400, \text{ and } 600\text{ °C}$ [13]. Hf thin films show a dome-shaped surface with fine to wide columnar structures, whereas Ti thin films display smooth to tableland-like surface structures with dense and wide columns. The Zr thin films deposited at 600 °C have structures that are a mixture of Ti and Hf thin films, featuring tableland-like flat surfaces. The Zr and Hf thin films deposited at $T_{\text{sub}} = 400$ and 600 °C are characterized by columns of uniform diameters on the surface. For all the materials, at $T_{\text{sub}}/T_m < 0.25$, the structure is categorized as Zone T, whereas at $0.25 < T_{\text{sub}}/T_m < 0.35$, the structure is categorized as Zone 2. The structure of the Ti thin films with $T_{\text{sub}}/T_m = 0.45$ is close to that of Zone 3, showing the crystallized shape of the surface. The changes in the lattice strain and reduced resistivity values demonstrate the zone transition as a function of T_{sub}/T_m . Figure 11 shows the lattice strains calculated from the shifts of Ti [(002) and (101)], Zr (002), and Hf (002) peaks obtained by X-ray diffraction (XRD) measurements as a function of T_{sub} and T_{sub}/T_m for the Ti, Zr, and Hf thin films, respectively [13]. The positive lattice strain indicates the compressive stress. The lattice strain of the Ti, Zr, and Hf thin films decreases at $T_{\text{sub}}/T_m = 0.25 - 0.30$ and then becomes constant or slightly decreases with T_{sub}/T_m [Fig. 11(b)]. Figure 12 shows the reduced resistivities (ρ/ρ_0) of the Ti, Zr, and Hf thin films as a function of T_{sub} and T_{sub}/T_m [13]. The ρ/ρ_0 values of the Ti and Zr thin films decrease with an increase in T_{sub} to 300 °C and $T_{\text{sub}}/T_m = 0.25 - 0.30$ and then sharply increase with an increase in T_{sub} and T_{sub}/T_m . However, the ρ/ρ_0 values of the Hf thin films monotonically decrease with an increase in T_{sub} . The ρ/ρ_0 curves for the Ti and Zr thin films show a clear bend at $T_{\text{sub}}/T_m = 0.25 - 0.30$. In the lattice strain and reduced resistivity plots, the bend point at $T_{\text{sub}}/T_m = 0.25 - 0.30$ for all the (Ti, Zr, and Hf) thin films is clearly shown, which corresponds to the transition across the boundary between Zone T and Zone 2. Hence, our data, which was systematically obtained according to the homologous substrate temperature, confirms the transitions of the film structures and properties at approximately $T_{\text{sub}}/T_m = 0.25 - 0.30$.

On comparison of the physical property graphs as a function of T_{sub} and T_{sub}/T_m , the graphs plotted against T_{sub}/T_m show a smaller deviation. Figure 13 shows the coefficient of determination (COD) obtained for the quadratic and exponential regressions of the physical

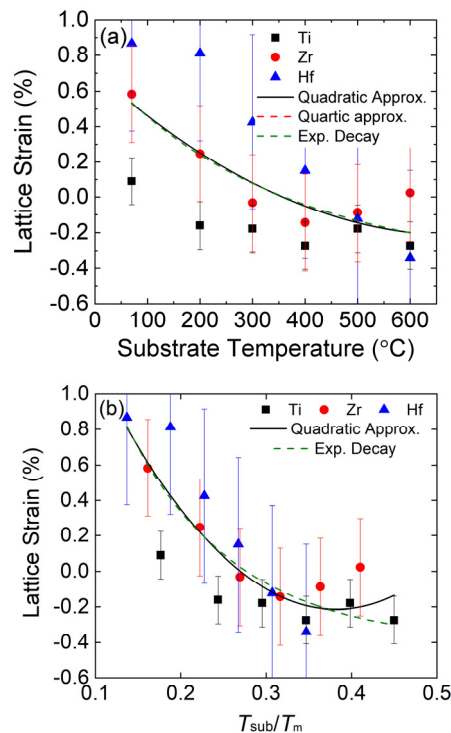


Figure 11. (Color online) Lattice strains calculated from the shifts of the Ti (002 and 101), Zr (002), and Hf (002) peaks obtained by XRD measurements as a function of T_{sub} and T_{sub}/T_m for Ti, Zr, and Hf thin films. The error bars indicate one standard deviation of uncertainty (Kusano [13]).

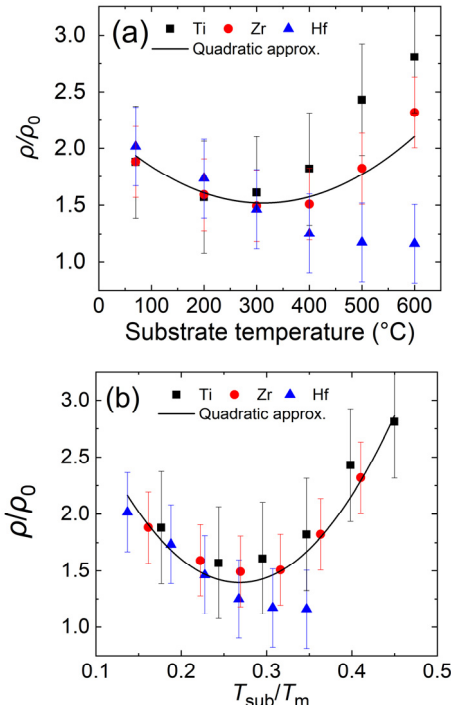


Figure 12. (Color online) Reduced resistivities of Ti, Zr, and Hf thin films as a function of (a) substrate temperature (T_{sub}) and (b) T_{sub}/T_m . The reduced resistivity is the ratio of the measured thin-film resistivity (ρ) to the bulk material resistivity (ρ_0). The error bars indicate one standard deviation of uncertainty (Kusano [13]).

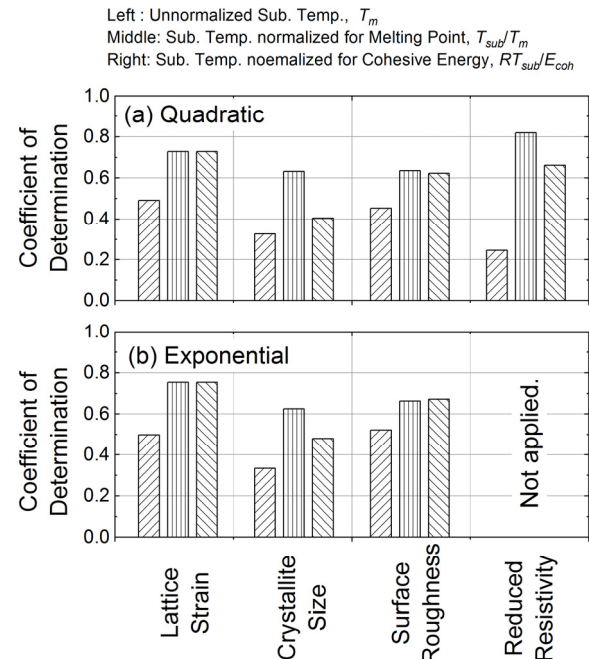


Figure 13. Coefficient of determination obtained for the (a) quadratic and (b) exponential regressions for the relationship between unnormalized substrate temperatures, substrate temperatures normalized with respect to the melting points T_{sub}/T_m , and substrate temperatures normalized with respect to the temperatures equivalent to the cohesive energies on lattice strain, crystallite size, surface roughness, and reduced resistivity (Kusano [13]).

property graphs plotted as a function of T_{sub} , T_{sub}/T_m , and $RT_{\text{sub}}/E_{\text{coh}}$, where R is the gas constant of $8.314 \text{ J K}^{-1} \text{ mol}^{-1}$ and E_{coh} denotes the cohesive energy [13]. For all film properties, the regressions of the plots against T_{sub}/T_m and $RT_{\text{sub}}/E_{\text{coh}}$ yield higher CODs compared with those obtained for the plots against the unnormalized T_{sub} . In particular, the regressions for the lattice strain and ρ/ρ_0 yield CODs higher than 0.7 for the plots against T_{sub}/T_m and $RT_{\text{sub}}/E_{\text{coh}}$. Hence, the effectiveness and appropriateness of the use of the homologous substrate temperature is well demonstrated by the results shown in Fig. 13.

The concept of the homologous substrate temperature in the SZM can be fundamentally applied to the deposition of compound thin films. Figure 14 shows the cross-sectional SEM images of the TiO_2 , ZrO_2 , and HfO_2 thin films deposited at $T_{\text{sub}} = 200, 400, 600$, and 800°C at the discharge pressure of 0.6 Pa [14]. The thin films deposited at $T_{\text{sub}}/T_m < 0.20$ exhibited columnar structures with fine voids and fine rough surfaces. In comparison, thin films deposited at $0.25 < T_{\text{sub}}/T_m < 0.32$ exhibited finer column structures with a flat surface, whereas those deposited at $0.35 < T_{\text{sub}}/T_m$ exhibited rougher or faceted surfaces. These changes represent the transition from Zone 1 to Zone 2. Compared with the SEM images of the metal films (Fig. 10), the transition of the zones for these metal oxide films (Fig. 14) is unclear. Figure 15 shows the lattice strains of the TiO_2 , ZrO_2 , and HfO_2 thin films as a function of T_{sub}/T_m . The positive lattice strain indicates compressive stress. The lattice strain was calculated from the shifts of the reflection peaks obtained by the XRD measurements [14]. The lattice strain of the metal oxide thin films decreases gradually with an increase in T_{sub}/T_m , reaching zero at $T_{\text{sub}}/T_m = 0.40, 0.26$, and 0.26 for the TiO_2 , ZrO_2 , and HfO_2 thin films, respectively. Figure 16 shows the

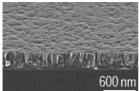
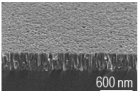
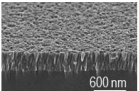
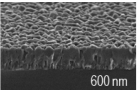
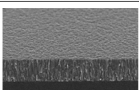
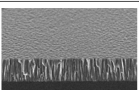
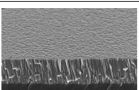
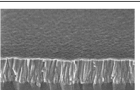
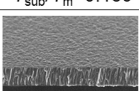
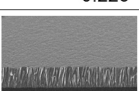

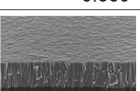
T_{sub}	200 °C	400 °C	600 °C	800 °C
TiO_2	 $T_{\text{sub}}/T_{\text{m}}=0.224$	 0.318	 0.413	 0.507
ZrO_2	 $T_{\text{sub}}/T_{\text{m}}=0.159$	 0.226	 0.292	 0.360
HfO_2	 $T_{\text{sub}}/T_{\text{m}}=0.154$	 0.219	 0.284	 0.349

Figure 14. Cross-sectional SEM images of TiO_2 , ZrO_2 , and HfO_2 thin films deposited at substrate temperatures of 200, 400, 600, and 800 °C (Kusano [14]).

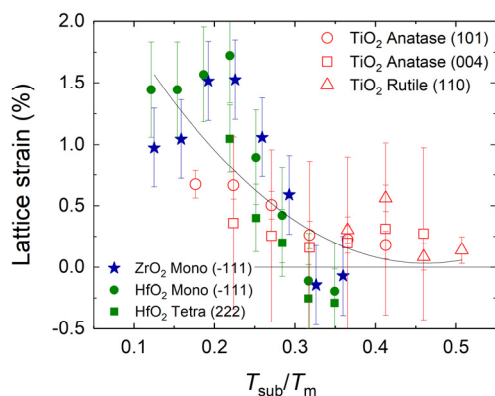


Figure 15. (Color online) Lattice strains calculated from the shifts of the TiO_2 (101) and (004) reflections of anatase and (110) reflections of rutile, monoclinic ZrO_2 (111), monoclinic HfO_2 (111), and tetragonal HfO_2 (222) as a function of $T_{\text{sub}}/T_{\text{m}}$. The dashed curve in the figure illustrates the exponential regression curve for the overall data. The error bars indicate half of the standard deviation of uncertainty (Kusano [14]).

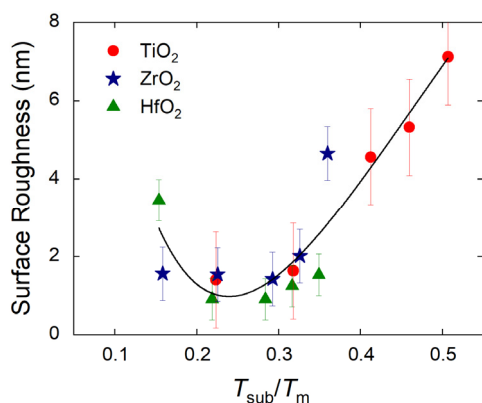


Figure 16. (Color online) Surface-roughness of TiO_2 , ZrO_2 , and HfO_2 thin films as a function of $T_{\text{sub}}/T_{\text{m}}$. The solid curve in the figure illustrates the exponential regression curve for the overall data. The error bars indicate half of the standard deviation of uncertainty (Kusano [14]).

surface roughness of the TiO_2 , ZrO_2 , and HfO_2 thin films as a function of $T_{\text{sub}}/T_{\text{m}}$ [14]. For the TiO_2 thin films, the surface roughness in-

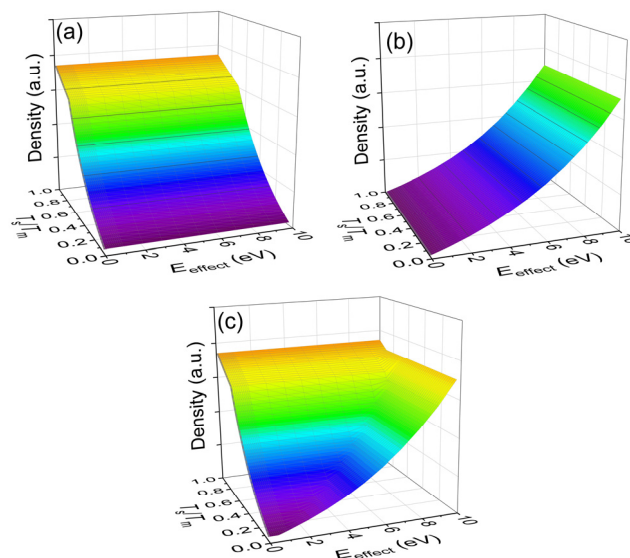


Figure 17. (Color online) Conceptual images of the evolved SZM as a function of (a) effective particle energy per depositing atom (E_{Effect}), (b) $T_{\text{sub}}/T_{\text{m}}$, and (c) the combination of (a) and (b).

creases sharply at $T_{\text{sub}}/T_{\text{m}} \geq 0.30$, whereas, for ZrO_2 and HfO_2 thin films, it decreases until $T_{\text{sub}}/T_{\text{m}} = 0.22$ and then increases with an increase in $T_{\text{sub}}/T_{\text{m}}$. For the lattice-strain changes of the TiO_2 , ZrO_2 , and HfO_2 thin films, the surface roughness increases with an increase in $T_{\text{sub}}/T_{\text{m}}$ showing a bend point at $T_{\text{sub}}/T_{\text{m}} \approx 0.25 - 0.28$. These results correspond to the boundary of the flat-to-faceted surface at $T_{\text{sub}}/T_{\text{m}} \approx 0.28 - 0.32$ shown in the SEM images (Fig. 14). The quantitative changes in the properties of the oxide films, such as crystallite size, lattice strain, and film surface roughness, show a transition at $T_{\text{sub}}/T_{\text{m}} \approx 0.30 - 0.35$. In correlation with the property transitions, thin film morphologies are categorized into Zone T and Zone 2. These results emphasize that the SZM is appropriate for compound thin films with thickness $< 1 \mu\text{m}$.

IV. SZM Evolution

In the SZM, the discharge-pressure axis represents the indirect effects of discharge pressure on the film texture, i.e., the interacted effects of the discharge pressure on the energy flux per depositing atom and the oblique incidence of particles depositing at the surface. Employing the energy flux instead of the discharge pressure will result in widely covering additional effects in the deposition process through the particle energization, as reported for the effects on the residual stress [20,21]. On this basis, the SZM has evolved with respect to energetic deposition [22-24]. Accordingly, the energy axis used in the evolved SZM should represent the energy effectively transferred to the growing film surface per deposited atom by the incident particles, as discussed by Kusano and Kikuchi [25], because the total energy per arriving atom does not effectively measure the energy transferred to the growing film surface. Figures 17(a) and 17(b) show the effects of the effective particle energy per depositing atom and $T_{\text{sub}}/T_{\text{m}}$ on the film density, respectively. With respect to the relationships shown in Fig. 17, it is assumed that both effective particle energy and $T_{\text{sub}}/T_{\text{m}}$ independently affect the film density. When the two effects are combined, the modified SZM based on the energy flux and $T_{\text{sub}}/T_{\text{m}}$ is

obtained, as shown in Fig. 17(c). Although synergistic effects are not considered in the evolved SZM shown in Fig. 17(c), the film densification and crystallization are accelerated with the synergistic effects in reality. In addition, the evolved SZM does not distinguish between these two effects: (1) the high particle energy induced film-structure densification under a non-thermal-equilibrium condition, resulting in the deposition of a thin film with a high density and high residual stress, and a flattened surface, and (2) a high $T_{\text{sub}}/T_{\text{m}}$ induced film-structure densification and crystallization under a thermal-equilibrium condition, resulting in the deposition of a thin film with high density, low residual stress, and a faceted surface. In the evolved SZM shown in Fig. 17, only film density is shown as the resulting property; however, other film properties change as a result of the change in the contribution ratio to the film structure modification between the energy flux and $T_{\text{sub}}/T_{\text{m}}$, even if the film is dense. Furthermore, by replacing the discharge pressure axis with the effective particle energy axis, the parameter demonstrating the effect of the oblique incidence disappears from the SZM. Therefore, it is necessary to develop the SZM integrating the effects of the oblique incidence (shadowing effects), particle energy, and homologous substrate temperature for demonstrating the changes in the film property more precisely.

V. Conclusions

In this paper, the SZM for the sputter-deposited thin films was reviewed. This review demonstrated that the SZM provides a systematic model for the changes in film structure and properties of the sputter-deposited thin films as functions of discharge pressure and homologous substrate temperature for metal and oxide thin films with thickness $< 1 \mu\text{m}$. Although it is necessary to modify the SZM in order to accurately address the deposition conditions, it is effective to optimize the film deposition conditions for obtaining desired film structure and properties. The evolution of the SZM by replacing the axis of discharge pressure with that of the energy effectively transferred per particle to the growing film surface was also discussed for the sputter deposition using the intended particle energization such as ionization and pulsed sputtering. Indeed, a comprehensive understanding of the SZM is necessary to sputter-deposit thin films according to the desired film structures and properties, which may be helpful in improving the applicability of sputter deposition in various industrial applications.

References

- [1] D. W. Hoffman and R. C. McCune, *Handbook of Plasma Processing Technologies*, edited by S. M. Rossnagel, J. J. Cuomo, and W. D. Westwood (Noyes Publications, Park Ridge, USA, 1989), pp. 483–517.
- [2] W. D. Westwood, *Sputter Deposition* (American Vacuum Society, New York, USA, 2003), pp. 131–166.
- [3] E. S. Machlin, *Materials Science in Microelectronics I: The Relationships between Thin Film Processing and Structure* (Elsevier, Oxford, UK, 2005), pp. 55–96.
- [4] J. A. Thornton, *J. Vac. Sci. Technol.* 11, 666 (1974).
- [5] J. A. Thornton, *Ann. Rev. Mater. Sci.* 7, 239 (1977).
- [6] J. A. Thornton, *J. Vac. Sci. Technol. A* 4, 3059 (1986).
- [7] B. A. Movchan and A. V. Demchishin, *Phys. Met. Metallogr.* 28, 83 (1969).
- [8] S. Craig and G. L. Harding, *J. Vac. Sci. Technol.* 19, 205 (1981).
- [9] R. Messier, A. P. Giri, and R. A. Roy, *J. Vac. Sci. Technol. A* 2, 500 (1984).
- [10] C. R. M. Grovenor, H. T. G. Hentzell, and D. A. Smith, *Acta Metall.* 32, 773 (1984).
- [11] P. B. Barna and M. Adamik, *Thin Solid Films* 317, 27 (1998).
- [12] N. Kaiser, *Appl. Opt.* 41, 3053 (2002).
- [13] E. Kusano, *J. Vac. Sci. Technol. A* 36, 041506 (2018).
- [14] E. Kusano, *J. Vac. Sci. Technol. A* 37, 051508 (2019).
- [15] J. A. Thornton, *Thin Solid Films* 54, 23 (1978).
- [16] J. A. Thornton and J. L. Lamb, *Thin Solid Films* 119, 87 (1984).
- [17] T. Oya and E. Kusano, *Thin Solid Films* 517, 5837 (2009).
- [18] M. Sakamoto, E. Kusano, and H. Matsuda, *Thin Solid Films* 531, 49 (2013).
- [19] J. A. Thornton and D. W. Hoffman, *Thin Solid Films* 171, 5 (1989).
- [20] A. J. Detor, A. M. Hodge, E. Chason, Y. Wang, H. Xu, M. Conyers, A. Nicroo, and A. Hamza, *Acta Mater.* 57, 2055 (2009).
- [21] G. Abadias, E. Chason, J. Keckes, M. Sebastiani, G. B. Thompson, E. Barthel, G. L. Doll, C. E. Murray, C. H. Stossel, and L. Martinu, *J. Vac. Sci. Technol. A* 36, 020801 (2018).
- [22] P. J. Kelly and R. D. Arnell, *J. Vac. Sci. Technol. A* 16, 2858 (1998).
- [23] I. Petrov, P. B. Barna, L. Hultman, and J. E. Greene, *J. Vac. Sci. Technol. A* 21, S117 (2003).
- [24] A. Anders, *Thin Solid Films* 518, 4087 (2010).
- [25] E. Kusano and N. Kikuchi, *Thin Solid Films* 634, 73 (2017).